Applied Physics Letters

RESEARCH ARTICLE | JUNE 03 2014

Continuous operation of a monolithic semiconductor terahertz source at room temperature

Q. Y. Lu; N. Bandyopadhyay; S. Slivken; Y. Bai; M. Razeghi

Check for updates

Appl. Phys. Lett. 104, 221105 (2014)
https://doi.org/10.1063/1.4881182

View Online Export Citation

Articles You May Be Interested In

Widely tunable room temperature semiconductor terahertz sourc e

Appl. Phys. Lett. (November 2014)

Widely tunable terahertz source based on intra-cavity frequency mixing in quantum cascade laser array s

Appl. Phys. Lett. (June 2015)

Monolithic top emitting room temperature THz DFG QCL with index grating for wavelength selectio n

AIP Advances (October 2024)

02 June 2025 18:48:58

AIP Publishing

APPLIED PHYSICS LETTERS 104, 221105 (2014)

Continuous operation of a monolithic semiconductor terahertz source at room temperature

Q. Y. Lu, N. Bandyopadhyay, S. Slivken, Y. Bai, and M. Razeghi[a)]
Center for Quantum Devices, Department of Electrical Engineering and Computer Science, Northwestern University, Evanston, Illinois 60208, USA

THz technology is under intense study, fuelled by applications from biological sensing to astronomical detection.[1] However, the lack of compact, continuous wave (CW) THz sources working at room temperature with high power and wide spectral tuning range, becomes a major obstacle to the wide application of THz technology. GaAs-based THz quantum cascade lasers (QCLs) are powerful semiconductor THz sources in the 2–5 THz range capable of CW operation,[2,3] but cryogenic cooling is still a necessity. Just as viable are the current narrowband offerings based on nonlinear frequency mixing in nonlinear crystals with external pumping sources like Nd:YAG laser, diode lasers, and vertical external cavity surface emitting lasers (VECSELs).[4,5] These are also capable of CW emission at room temperature depending on the pumping sources. However, they require multiple optical components to function.

On the other hand, the mid-infrared (mid-IR) QCL technology is developing rapidly and becoming the leading semiconductor source in the mid-IR range.[6–8] The QCL is able to not only produce high power high efficiency mid-IR emission but also possesses a giant nonlinearity for THz difference-frequency generation (DFG).[9] With a proper wavelength selection mechanism, such as the composite distributed feedback (DFB) for dual mid-IR wavelength operation, a narrow-band THz emission can be intracavity generated.[10] Therefore, this type of terahertz source inherits the advantage of the mid-IR QCLs, such as room temperature operation, electrical pumping, compact size, as well as potential for mass production.

While efforts has been devoted to improve the THz power[11,12] and frequency tuning range[12–14] of THz sources based on DFG QCLs, the capability of CW operation at room temperature is of utter importance to wide application and commercialization. Room temperature CW operation has not been achieved for the following reasons. First, the design priority has been to achieve for a large nonlinear susceptibility ($v^{(2)}$) for THz generation. However, this may compromise the mid-IR performance. Second, to obtain a large population inversion for large $v^{(2)}$, the doping of the structure is much higher than a typical mid-IR QCL, which results in a high threshold current density, precluding room temperature CW operation. Third, to obtain high peak power, the waveguide structure is often wider than a typical mid-IR QCL, which poses a big challenge for thermal management. In this work, we address the structure design, doping, and thermal management all together and demonstrate the first room temperature CW THz source based on DFG in QCLs. Room temperature single mode emissions at 3.6 THz with a power of 3lW and a mid-IR-to-THz conversion efficiency of 0.44 mW/W^2 are obtained in continuous wave mode. THz peak power up to 1.4 mW in pulsed mode operation with a conversion efficiency of 0.8 mW/W^2 at 3.5 THz is also demonstrated through scaling up the mid-IR power.

In spite of the high peak powers achievable in mid-IR QCLs, the limiting factor for CW operation of DFG THz sources based on QCLs at room temperature is internal heating. These THz sources in the recent demonstrations have an input electrical power density $J_{th} V_{th}$ of about 120kW/cm^2, which is too high for CW operation. Here, J_{th} and V_{th} are threshold current density and voltage, respectively. Typical CW mid-IR QCLs operate at a much lower power density of 20kW/cm^2. For this reason, it is essential to minimize the threshold current density and voltage. This can most readily be achieved by lowering the waveguide loss and the laser core doping density. It is also beneficial to increase the device thermal conductance, in order to better dissipate heat.

The waveguide of our THz device is grown on a semiinsulating InP substrate in order to utilize the Cerenkov phase matching scheme. In addition to epilayer-down mounting on patterned submounts and use of a double-sided current injection strategy,[11] the waveguide is further improved in the following aspects in order to increase the thermal conductance and decrease the waveguide loss. The first is the realization of a narrow-stripe, planarized, buried heterostructure geometry within the double-side injection structure. This architecture has both high thermal conductance and low loss and is widely used for the high performance CW mid-IR QCLs.[15,16] Physically, the narrow gain region (12lm) is

completely surrounded by InP, which serves as the waveguide cladding. Compared to previous efforts that utilized

a)
Electronic mail: razeghi@eecs.northwestern.edu

0003-6951/2014/104(22)/221105/5/$30.00 104, 221105-1 Vc 2014 AIP Publishing LLC

(Received 17 April 2014; accepted 21 May 2014; published online 3 June 2014)

We demonstrate room temperature continuous wave THz sources based on intracavity difference-frequency generation from mid-infrared quantum cascade lasers. Buried ridge, buried composite distributed-feedback waveguide with Cerenkov phase-matching scheme is used to reduce the waveguide loss and enhance the heat dissipation for continuous wave operation. Continuous emission at 3.6 THz with a side-mode suppression ratio of 20dB and output power up to 31W are achieved, respectively. THz peak power is further scaled up to 1.4 mW in pulsed mode by increasing the mid-infrared power through increasing the active region doping and device area. Vc 2014 AIP Publishing LLC. [http://dx.doi.org/10.1063/1.4881182]

02 June 2025 18:48:58

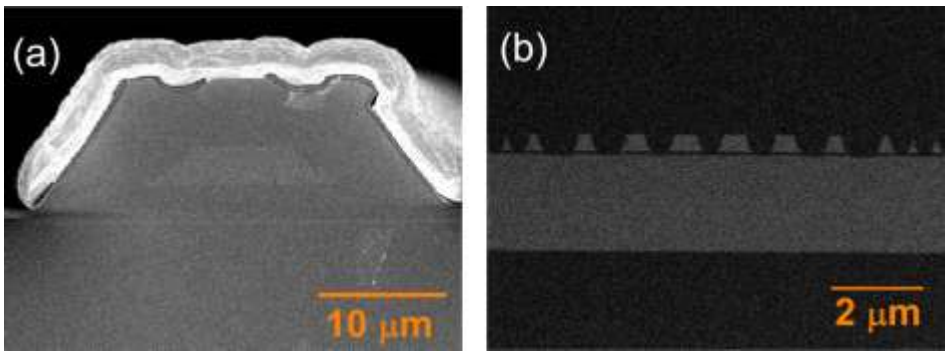

FIG. 1. Scanning electron microscope (SEM) images of the buried ridge (a), buried composite DFB gratings (b).

widths of 20lm, the thermal conductance will be increased by 80%. After the planarization step to form the buried heterostructure, a wider ridge (32lm) is then formed around this waveguide with double-sided current injection by etching through all waveguide layers down to the bottom contact layer. Laterally, the gain region is about 10lm away from the metal layers in order to minimize the waveguide loss, as shown in Fig. 1(a).

The second is the use of a buried composite DFB grating within the waveguide for mid-IR wavelength selection. The composite grating is built from the superposition of two different gratings with independent periodicity.[10] This allows for simultaneous multiple wavelength operation within the laser cavity. In previous work, the grating was fabricated in the InP cap layer (surface grating). In order to obtain a sufficient coupling strength, the top cladding layer was relatively thin (3–3.5lm), which induced a high waveguide loss (6–10cm^{1}) in the mid-IR operating wavelength range (8–12lm) due to strong free-carrier absorption. In the present work, the composite grating is defined into a 500-nm InGaAs layer located on the top of the gain region, as shown in Fig. 1(b), with a 6lm thick upper waveguide cladding. Each wavelength component of the composite grating has a duty cycle of 35% in order to achieve an estimated coupling coefficient of j 25–30cm^{1} for both grating components. Due to this strong coupling, the grating is only patterned on the rear half section of the cavity. Thanks to both the buried ridge and buried DFB designs, the waveguide loss is drastically reduced to an estimated 1–2cm^{1}.

QCLs active region features two single-phonon resonance (SPR)[13] cores designed with wavelengths of 8.9 and 10lm is used. Given a waveguide loss of 1.5cm^{1} and mirror loss of 1.8cm^{1} for a 4-mm long cavity with high-reflection (HR) coating, $v^{(2)}$ is estimated to be 2.610^{4} pm/V. This is lower than 3.810^{4} pm/V of the previous ridge waveguide with a waveguide loss of 8cm^{1} and a mirror loss of 2.7cm^{1} from an HR coated 3-mm cavity. The lower $v^{(2)}$ is related to the reduced threshold gain and the population inversion DN necessary for laser oscillation.

The QCL structure presented in this work is based on the lattice-matched $In_{0.53}Ga_{0.47}As/In_{0.52}Al_{0.48}As$ material system grown by gas-source molecular beam epitaxy on a semi-insulating InP substrate. The growth started with a 200-nm InGaAs layer (Si, 110^{18} cm^{3}), and 3-lm InP buffer layer (Si, 210^{16} cm^{3}). The laser cores consisted of two 20-stage SPR structures designed for the two wavelengths, respectively. The average doping is about 2.510^{16} cm^{3}. The sample is processed into a buried composite DFB and buried ridge waveguide with ridge width of 12lm and cleaved into 4mm long cavity. After HR coating on the rear facet, the front facet is polished with an angle of 30. Then, the device is epilayer-down mounted on a patterned diamond submount. For pulsed mode testing, a pulse width of 200ns with different duty cycles (duty cycle¼pulse width/pulse period) are used. Figure 2(a) is the average optical power-current-voltage (P-I-V) characterizations of a 4-mm long DFB device with a 12lm ridge width under pulsed mode operation at different duty cycles. The average output power is the direct reading from the thermopile without any correction. CW operation corresponds to a duty cycle of 100%. All testing is performed at 293K. The P-I-V curves of a Fabry-Perot (FP) device with the same geometry under CW operation are also presented. In pulsed mode

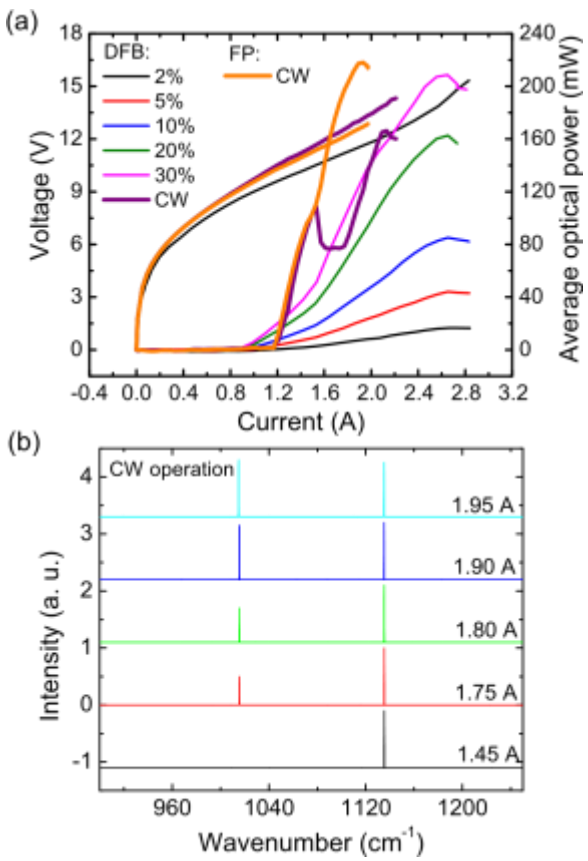

FIG. 2. (a) P-I-V characterization of a composite DFB device in pulsed mode and CW operation, together with P-I-V characterization of a FP device in CW operation. (b) Mid-IR spectra of a composite DFB device in CW operation at different currents. The frequency spacing corresponds to 3.6 THz.

operation, the DFB device exhibits a peak power (average power divided by the duty cycle) up to 880 mW at 5% duty cycle and a threshold current density of 1.83kA/cm^{1}, while the FP device exhibits a slightly higher threshold current density of 1.88kA/cm^{1} and a higher peak power of 1.1W. The average powers for both devices increase consistently at low duty cycle

02 June 2025 18:48:58

(<30%) and saturate above 40% duty cycle. In CW operation, the DFB device emits up to 165 mW with a threshold current density of 2.44kA/cm[1]. A prominent kink in a current range of 1.5–1.7A in the P-I curve is observed. The lasing spectrum measurement indicates that this kink is related to the transition from single wavelength operation to dual wavelength operation. The FP device emits a CW power up to 218 mW with a similar threshold current density of 2.43kA/cm^2 and does not have an obvious kink. Figure 2(b) is the CW lasing spectra from 1.45A to 1.95A. Single mode operation at k_1 ¼8.81lm and k_2 ¼9.85lm with a frequency spacing of 3.6 THz is observed from 1.6A up to the rollover at 2A. The spectrum in CW operation is red-shifted by about 6.5 and 7.5cm[1] for the two wavelengths with respect to the pulsed mode spectrum due to the heating effect.

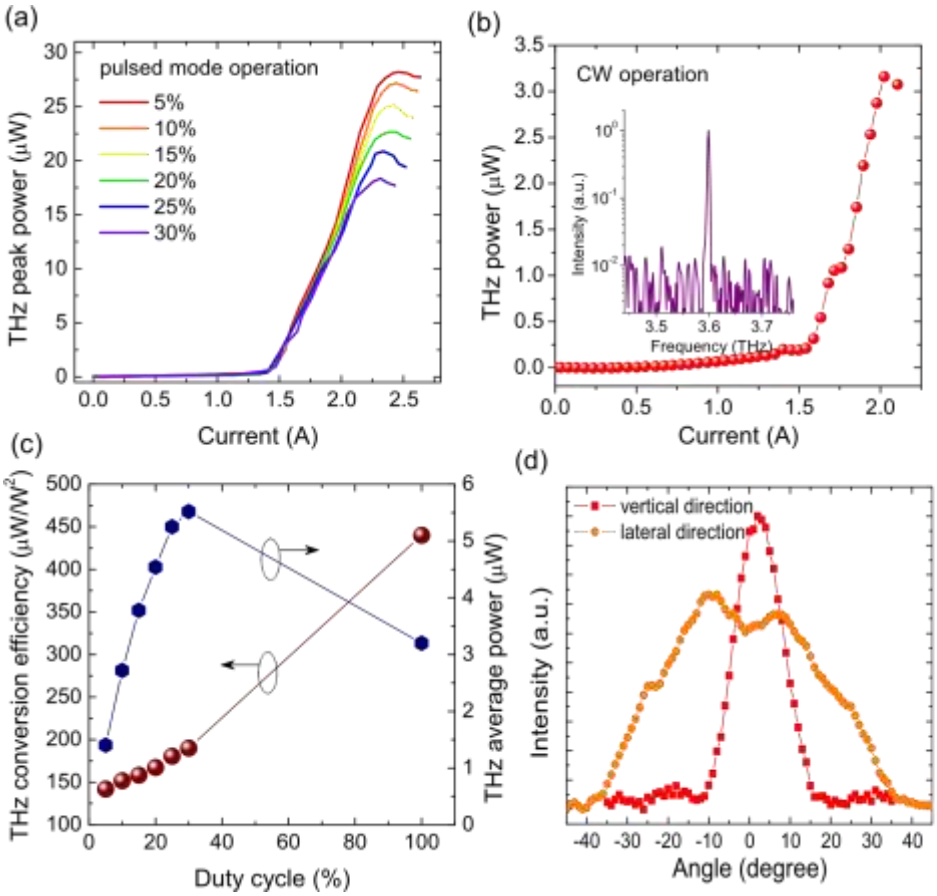

FIG. 3. (a) THz peak power as functions of current at different pulsed duty cycles. (b) THz CW power as a function of current and CW emitting spectrum at 3.6 THz at a current of 1.9 A (inset). (c) THz conversion efficiency and average power as functions of current duty cycle. (d) THz far fields in vertical and lateral directions at a current of 1.9 A with 25% duty cycle.

THz power is tested with a Golay cell detector (Microtech Instruments). For CW THz power testing, the device is actually modulated with a low frequency pulse (quasi-CW, 40ms pulse width and 12.5Hz repetition rate) in order to be compatible with Golay cell detection. Since the pulse duration is much longer than the thermal stabilization time in QCL (<100 ls), there should be minimal difference in power compared to a true CW operation. Figure 3(a) is the THz peak powers in pulsed mode operation tested with different duty cycles from 5% to 30% at 293K. The power value is not corrected for collection efficiency. A maximum peak power of 28lW at 5% and a maximum average power of 5.5lW at 30% are obtained. The mid-IR-to-THz conversion efficiencies are 142 and 190lW/W^2, respectively. Following with a clear increasing trend in conversion efficiency with duty cycle, the CW THz power reaches 3lW with a conversion efficiency of 0.44 mW/W^2 (Fig. 3(b)).

As discussed before, for a given active structure, the nonlinear optical coefficient $v^{(2)}$ is susceptible to the change of population inversion DN which is estimated at the threshold condition where the net gain equals the total loss. As the internal temperature increases with the duty cycle, the broadening of the optical response and increased free-carrier losses[17] leads to a higher threshold and DN. Thus, a higher nonlinearity and a higher conversion efficiency are inferred at high duty cycles and CW operation, as shown in Fig. 3(c) (red curve). On the other hand, the dramatic decrease in the mid-IR power from pulsed to CW operation is responsible for the gradual decrease of THz average power from 5.5lW at 30% duty cycle to 3lW at CW as shown in Fig. 3(c) (blue curve).

The THz spectra are tested with a Bruker Fourier transform infrared (FTIR) spectrometer equipped with an uncooled far-IR deuterated L-alanine doped triglycine sulfate (DTGS) detector. In the experiment, the THz CW spectra were scanned from 1.7 to 2.0A with a step of 50mA, when the device was biased with CW currents without any modulations. The total spectral testing time lasted for minutes due to the slow response of the far-IR DTGS detector. The side mode suppression ratio (SMSR) is about 20dB at a CW current of 1.9A as shown the inset of Fig. 3(b). The linewidth is 5GHz, which is mainly limited by the resolution (3.7GHz) of the FTIR. Note that the intrinsic THz linewidth should be on the order of hundreds of Hz since the THz device is based on the CW operation of the mid-IR QCL which is already measured with hundreds of Hz linewidth.[18] The THz far field is

02 June 2025 18:48:58

measured by mounting the device on a computer controlled rotational stage and recording the signal with a Golay cell detector. Figure 3(d) presents the THz far field distributions at 1.9A with 25% duty cycle. Divergence angles are 13.5 and 45 in the vertical and lateral directions (x-z and y-z planes), respectively.

With a similar optimization process, the THz peak power in pulsed mode is further scaled up by increasing the mid-IR power and conversion efficiency. A second wafer with two 30-stage SPR structures, a higher doping (710^{16} cm^3) in the active region, and a thinner cladding layer of 3lm for strong surface DFB coupling is processed into 24lm wide ridge waveguide and cleaved into 3mm long laser bar. Figure 4(a) is the mid-IR P-I-V characterization of a device epilayer-down mounted and tested in pulsed mode with 60ns pulse width and 1% duty cycle at 293K. A peak power up to 2.6W and a threshold current density of 8.1kA/cm[1] are obtained. Stable dual wavelength operation with k_1 ¼8.93lm and k_2 ¼9.98lm is observed up to the rollover current, as shown in the inset of Fig. 4(a). After polishing the front facet at a 30 angle, a maximum THz peak power of 1.4 mW is achieved from this device, as presented in Fig. 4(b). The corresponding conversion efficiency is 0.8mW/W^2. The increased the THz peak power and conversion efficiency is attributed to the high active region doping and broader device area. The THz wall plug efficiency (WPE) of this device is estimated to be 0.510^5. Both the THz power and WPE are about one order magnitude higher than the values in previous demonstrations.[11,12] By enlarging the outcoupling aperture with a Si prism to allow for more THz light to be coupled out from the cavity or replacing the InP-substrate with less lossy Si substrate, even higher THz power and efficiency in a wider spectral range in pulsed and CW modes can be obtained. This is of special importance to high THz frequency generation (>4.5THz), where the phonon absorption in the semi-insulating InP substrate plays a leading role to the THz absorption in the substrate.

Spectral emission is single mode at 3.5 THz wish SMSR as high as 30dB as shown in the inset of Fig. 4(b). The far field testing indicates that the device exhibits a good beam profile with divergence angles of 12.5 and 36 in vertical and lateral directions. The peak position in vertical direction is at 5, which is different from the peak position at þ2 for the CW device at 3.6 THz. This difference is related to a change in the Cerenkov angles induced by the different refractive indices for the two lasers and the uncertainty of the manually polished facet angle. In both cases, a dual-peak distribution in the lateral direction is observed, with peak-to-peak angles of 19 and 16 for this high peak power device and the CW device. Note the ideal far field pattern of the Cerenkov THz emission inside of the waveguide should be a conical shape with the cone angle equal to the Cerenkov angle, [19] as shown in Fig. 4(d). Since only part of this radiation cone is able to be coupled out through the polished substrate facet limited by the Brewster's angle, the lateral beam pattern should exhibit a crescent-like beam shape. As the peak position in the vertical direction diverts from 0, a dual peak pattern in the lateral far field is observed, as shown in Figs. 3(d) and 4(c). Careful polishing of the facet into a lens shape in the lateral direction may able to reshape the THz beam with a small divergence angle, it also may enhance the THz outcoupling efficiency by emitting larger portion of the Cerenkov cone.

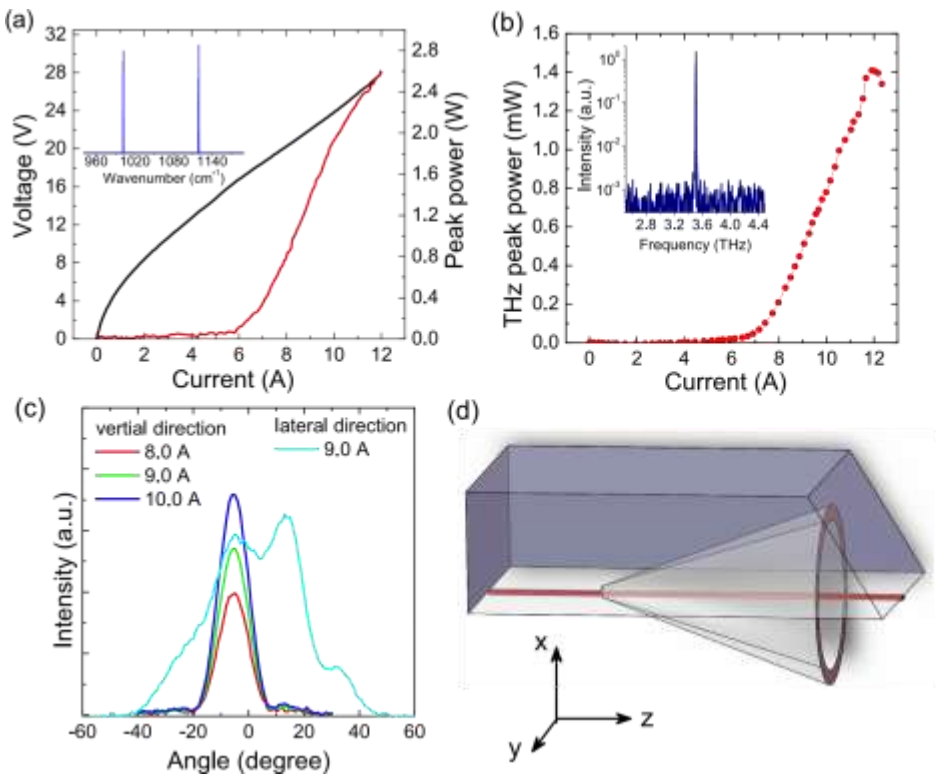

FIG. 4. (a) P-I-V characterization of a wide-ridge DFB device in pulsed mode operation. Inset is the mid-IR spectrum at 10 A. (b) THz peak power as a function of current and emitting spectrum at 10 A (inset). (c) THz far field distributions in vertical direction at different currents and lateral direction at 10 A. (d) Schematic of THz emission based on Čerenkov phase matching inside of the waveguide.

In conclusion, we report the room temperature CW THz sources at 3.6 THz with a side-mode suppression ratio of 20dB and output power up to 3lW. The CW THz power can be further enhanced by improving the mid-IR efficiency and power with a strain-balanced active region design and a longer

02 June 2025 18:48:58

cavity design. Furthermore, the THz peak power is scaled up to 1.4 mW in pulsed mode at room temperature with a mid-to-THz conversion efficiency of 0.8 mW/W^2. This is achieved by increasing the mid-IR power through scaling of the active region doping and device area. A record high THz wall plug efficiency of 0.5[10][5] is obtained.

This work is partially supported by the National Science Foundation (grants ECCS-1231289 and ECCS-1306397), Department of Homeland Security (grant HSHQDC-13-C00034), Naval Air Systems Command (grant N68936-13-C0124), and an Early Stage Innovations grant from NASA's Space Technology Research Grants Program. The authors would also like to acknowledge the encouragement and support of all the involved program managers.

[1] B. Ferguson and X. C. Zhang, Nature Mater. 1, 26–33 (2002).
[2] R. K€ohler, A. Tredicucci, F. Beltram, H. E. Beere, E. H. Linfield, A. G. Davies, D. A. Ritchie, R. C. Iotti, and F. Rossi, Nature 417, 156 (2002).
[3] B. S. Williams, S. Kumar, Q. Hu, and J. L. Reno, Electron. Lett. 42, 89–90 (2006).
[4] W. Shi and Y. J. Ding, Opt. Lett. 30, 1030–1032 (2005).
[5] M. Scheller, J. M. Yarborough, J. V. Moloney, M. Fallahi, M. Koch, and S. W. Koch, Opt. Express 18, 27112–27117 (2010).
[6] J. Faist, F. Capasso, D. L. Sivco, C. Sirtori, A. L. Hutchinson, and A. Y. Cho, Science 264, 553–556 (1994).
[7] M. Razeghi, "High-performance InP-based mid-IR quantum cascade lasers," IEEE J. Quantum Electron. 15, 941 (2009).
[8] Y. Yao, A. J. Hoffman, and C. F. Gmachl, Nat. Photonics 6, 432 (2012).
[9] M. A. Belkin, F. Capasso, F. Xie, A. Belyanin, M. Fischer, A. Wittmann, and J. Faist, Appl. Phys. Lett. 92, 201101 (2008).
[10] Q. Y. Lu, N. Bandyopadhyay, S. Slivken, Y. Bai, and M. Razeghi, Appl. Phys. Lett. 99, 131106 (2011).
[11] Q. Y. Lu, N. Bandyopadhyay, S. Slivken, Y. Bai, and M. Razeghi, Appl. Phys. Lett. 103, 011101 (2013).
[12] K. Vijayraghavan, Y. Jiang, M. Jang, A. Jiang, K. Choutagunta, A. Vizbaras, F. Demmerle, G. Boehm, M. C. Amann, and M. A. Belkin, Nat. Commun. 4, 2021 (2013).
[13] Q. Y. Lu, N. Bandyopadhyay, S. Slivken, Y. Bai, and M. Razeghi, Appl. Phys. Lett. 101, 251121 (2012).
[14] Q. Y. Lu, N. Bandyopadhyay, S. Slivken, Y. Bai, and M. Razeghi, Opt. Express 21, 968 (2013).
[15] Y. Bai, S. Slivken, S. R. Darvish, and M. Razeghi, Appl. Phys. Lett. 93, 021103 (2008).
[16] A. Lyakh, R. Maulini, A. Tsekoun, R. Go, C. Pflugl, L. Diehl, Q. J. Wang, F. Capasso, and C. K. N. Patel, Appl. Phys. Lett. 95, 141113 (2009).
[17] F. Carosella, C. Ndebeka-Bandou, R. Ferreira, E. Dupont, K. Unterrainer, G. Strasser, A. Wacker, and G. Bastard, Phys. Rev. B 85, 085310 (2012).
[18] L. Tombez, J. D. Francesco, S. Schilt, G. D. Domenico, J. Faist, P. Thomann, and D. Hofstetter, Opt. Lett. 36, 3109–3111 (2011).
[19] K. Chikuma and S. Umegaki, J. Opt. Soc. Am. B 7, 768–775 (1990).

02 June 2025 18:48:58